A Fault Clearing Method in Converter-Dominated Microgrids With Conventional Protection Means

Konstantinos O. Oureilidis, *Member, IEEE*, and Charis S. Demoulias, *Senior Member, IEEE*

***Abstract*—The integration of converter-interfaced distributed generation in microgrids has raised several technical issues, including the successful operation of protective devices during faults. The protection issue is associated with the lack of large current injection during a fault, due to limits imposed by the semiconductor switches. This paper proposes a fault-detection and clearing control strategy method for symmetrical and asymmetrical line faults in a looped microgrid. The protection devices are simple overcurrent devices with the same settings, due to the looped microgrid topology. The proposed method is applied without using any kind of physical communication. The fault is detected by measuring indirectly the microgrid impedance. After the fault identification, the distributed energy resources (DERs) adjust their control in order to inject a current proportional to the measured microgrid impedance, according to a droop curve. This means that the DER closer to the fault injects a relatively larger current, achieving by this way a selective coordination of the protection means. The effectiveness of the proposed control strategy is evaluated through detailed simulation and experimental tests.**

***Index Terms*—Distributed energy resources (DERs), droop control, microgrid protection, overcurrent devices.**

I. Introduction

THE microgrid is considered as a new approach of power generation and delivery system that contains converter-interfaced distributed energy resources (DERs) and loads, along with traditional rotating machines, forming a small controllable subsystem [1]. The subsystem should be able to operate either grid-connected or isolated depending on factors, such as the unavailability of the main grid or economic reasons. Due to the renewable energy growth, the microgrids present a high proliferation of dc/ac and ac/dc/ac converters [2]. In order to capitalize their benefits, the converter-interfaced DERs are required to conduct several operations, including the proper voltage and frequency control, the power demand sharing, the fault ride through capability, and the seamless transition between the operation modes. These requirements present new challenges to meliorate the control strategy and tackle with the protection issues in microgrids consisting of converter-interfaced sources [3].

When the microgrid operates islanded in steady-state mode, the active and reactive power of the connected DERs can be determined by the frequency and the voltage magnitude of the common ac bus, respectively, through the principles of the droop control philosophy [4]. Therefore, a high-quality voltage is ensured in each node of the microgrid, without any kind of extra physical communication among the DERs [5].

In case of a fault within a microgrid, the converter-interfaced DERs are not able to contribute with large currents, as rotating machines do [6], [7]. The fault-current capability of a converter-interfaced DER is limited by the short-time current carrying capacity of the semiconductor switches. The protection problem is even more severe in case of grid absence. In grid-connected mode, a large current can be fed from the main grid in order to detect and clear the fault [8], [9]. Previous published works propose the disconnection of the distributed generation during the fault [10], [11]. However, such a practice cannot be adopted in the modern grids, due to the high penetration of the converter-interfaced distributed generation.

In the literature, the available protection techniques are based either on communication, local measurements, or the use of external devices. The communication-based methods solve the protection problem by adjusting automatically the relay settings by means of online communication systems [12]–[16]. In [12], an extensive communication infrastructure is needed in order to update the relays' settings in an adaptive way, while in [13] a Central Protection Unit is also added. In differential protection [14], [15], a methodology for setting the differential relays properly is proposed, while in [15], communication-assisted relays are used. In overcurrent protection [16], the fault event is recognized by local measurements and is cleared by interbreaker communication means. The settings of the relay are again updated by a supervisory controller. The drawback of these methods is that the possible configurations of the microgrid should be known before the protection implementation [17]. On the other hand, other methods use new type of relays based on local measurements, without the necessity of communication. In [18], the voltage magnitude is used to recognize the fault, and in [19], the current is measured by utilizing the principles of synchronized phasor measurements. In [20], the distance from the fault is calculated by measuring the line admittance, in order to change the relay settings properly without any need for communication, while in [21], the coordination of digital relays based on wavelet packet transform is used for detecting and clearing the faults. Finally, there are methods that propose the use of external devices, such as energy storage systems with high fault current capability (e.g., flywheels) [22] and fault current limiters [23]. The latter methods, as well as the differential methods, are still considered as very expensive protection solutions.

This paper proposes a novel symmetrical and asymmetrical fault-detection and clearing process for looped microgrids with converter-interfaced DERs, without using expensive protective devices or physical communication link. The fault clearing is carried out by the coordination of simple overcurrent protection devices (OPD). Due to the looped topology of the microgrid, the loads can be placed arbitrarily; thus, each OPD should have

Manuscript received April 8, 2014; revised December 5, 2014 and June 26, 2015; accepted August 31, 2015. Date of publication September 14, 2015; date of current version January 7, 2016. Recommended for publication by Associate Editor Q.-C. Zhong.

The authors are with the Electrical Machines Laboratory, Department of Electrical and Computer Engineering, Aristotle University of Thessaloniki, Thessaloniki P.C. 54124, Greece (e-mail: oureili@yahoo.gr; chdimoul@auth.gr).

Color versions of one or more of the figures in this paper are available online at http://ieeexplore.ieee.org.

Digital Object Identifier 10.1109/TPEL.2015.2476702

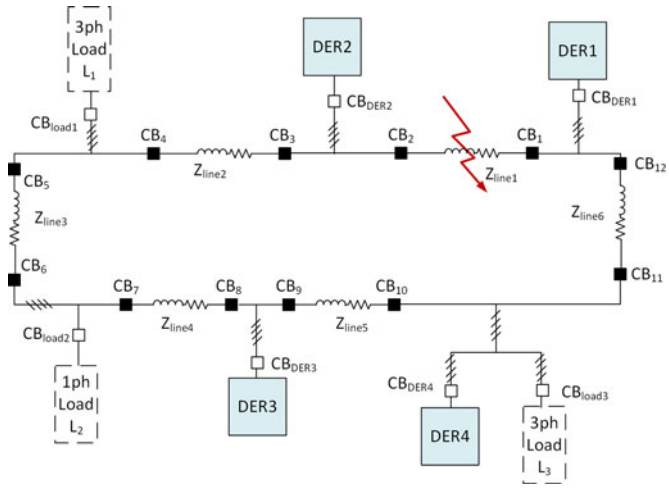

Fig. 1. Microgrid simulation model.

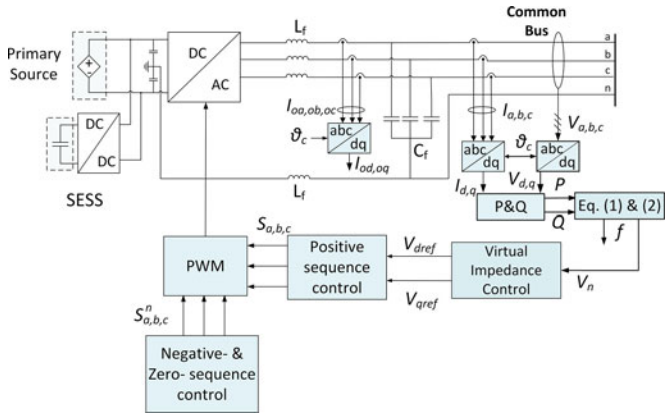

Fig. 2. DER basic control strategy scheme.

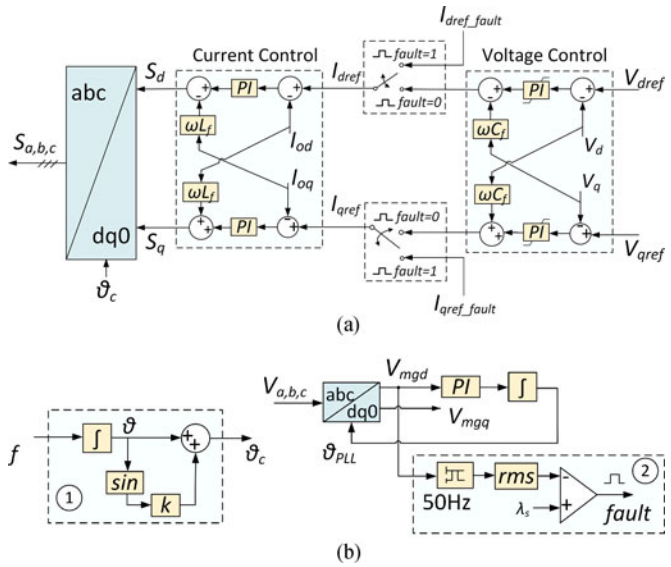

Fig. 3. (a) Positive sequence control strategy. (b) ① Angle distortion control and ② Fault-detection control.

the same rating. As a result, selectivity during the faults cannot be achieved through the settings of the OPDs. In order to introduce some selectivity, the OPDs closer to a fault should sense a current larger than the other OPDs. In order to achieve this, the DERs closer to the fault should inject relatively larger currents than the ones farther from it. According to the proposed method, each DER identifies a fault by calculating indirectly the microgrid impedance at its terminals. When the calculated impedance drops below a threshold, the fault is detected. Consequently, the control strategy is switched from the steady-state operation to the fault operation mode, where each DER is controlled to inject a fault current proportional to the microgrid impedance according to a new droop curve. Therefore, the DERs closer to the fault (i.e., the DERs sensing a smaller impedance) inject a relatively larger current. Since OPDs are assumed to be equipped with either extremely inverse time-current [24] or I^2t characteristics [25], [26], the proposed fault-detection and clearing method has certain limitations, which are clearly described in the paper. The method for calculating the droop curve coefficient from the microgrid topology is also presented. In order to ensure large enough current injection, even in case of using a renewable energy source, a supercapacitor energy storage system is connected in the dc link of each DER.

The proposed technique is tested for line faults in a looped converter-interfaced microgrid, as shown in Fig. 1. The loads are implemented as three-phase and single-phase RL elements, while the primary source of the DERs is considered a renewable energy (e.g., photovoltaic source). The control strategy implementation is described in detail in Section II, while Section III presents the simulation results, proving the effectiveness of the proposed control for both symmetrical and asymmetrical faults. Finally, in Section IV, the proposed control strategy is tested in a small-scale laboratory microgrid for a three-phase to ground and a two-phase to ground fault.

II. Control Strategy

A. Steady-State Operation

When an islanded microgrid operates in steady state, the active and reactive power of the DERs is determined by the droop control method, emulating the operation of a synchronous generator. According to this control strategy, the frequency and magnitude of the output voltage is controlled by the active and reactive power, respectively, as described in (1) and (2):

$$f = f^* - m \cdot P - m_d \frac{dP}{dt} \tag{1}$$

$$V_n = V^* - n \cdot Q - n_d \frac{dQ}{dt} \tag{2}$$

where f^* and V^* correspond to the frequency and magnitude of the output voltage at no load, m and n to the droop coefficients, P and Q to the average active and reactive power, and m_d and n_d to the derivative droop coefficients, respectively. The active and reactive power are calculated by the d,q parameters of the measured three-phase current and voltage at the output filter of the dc/ac converter according to Park transformation, as it is illustrated in Fig. 2.

The droop control methodology consists of a voltage and current controller [5], shown in Fig. 3. Initially, the reference voltages V_{dref} and V_{qref} are generated from the virtual impedance control, as presented in Fig. 2, in order to minimize the circulating currents among the connected DERs [27], [28]. These

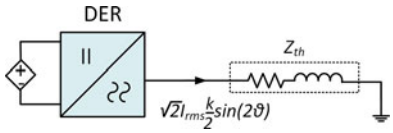

Fig. 4. Thevenin equivalent circuit for the double-frequency component.

voltage references ($V_{d\mathrm{ref}}$ and $V_{q\mathrm{ref}}$) serve as inputs in the voltage controller. The outputs of this controller are actually the references $I_{d\mathrm{ref}}$ and $I_{q\mathrm{ref}}$, which are inserted in the current controller as inputs. It should be mentioned that under steady-state conditions, the signal "fault" = 0. Finally, the output of the current controller S_d and S_q are transformed through *dq/abc* Park Transformation to $S_{a,b,c}$, which are the pulse width modulation (PWM) signals.

B. Fault-Detection Algorithm

The fault detection is based on the indirect calculation of the microgrid impedance at the output of each DER. Each DER injects intentionally—by changing the control angle—a disturbance signal in the current and measures its feedback in the voltage at the point of connection with the microgrid bus, through a phase-locked loop (PLL). When a fault occurs inside the microgrid, the feedback signal takes a value below a predefined threshold λ_s, resulting in the fault detection.

The magnitude of the disturbance signal is equal to the magnitude of the injected current, while its phase is selected so as not to affect its zero-crossing. The initial control angle is calculated from the droop control as a function of frequency f

$$\theta = \int 2\pi f dt. \tag{3}$$

The new control angle θ_c can be calculated by adding to the initial angle θ a quantity proportional to $\sin\theta$, as described by

$$\theta_c = \theta + k\sin\theta. \tag{4}$$

The gain k is selected to be quite small in order not to increase the harmonic content of the current. The angle distortion control scheme is implemented as in Fig. 3(b). This angle distortion has also been used in [29] as an active antiislanding method, implemented in a grid-connected single-phase photovoltaic converter. The equation of the current of phase a can be defined as

$$I_a = \sqrt{2}\cdot I_{\mathrm{rms}}\sin(\theta + k\sin\theta). \tag{5}$$

Assuming that the quantity $k\sin\theta$ is very small, then $\cos(k\sin\theta) \approx 1$ and $\sin(k\sin\theta) \approx k\sin\theta$; thus, (5) can be transformed to

$$I_a = \sqrt{2}I_{\mathrm{rms}}(\sin\theta + \frac{k}{2}\sin 2\theta). \tag{6}$$

As it can be deduced, the current consists of two components: the first is the same as in normal operation, while the second assigns to the disturbance. The effect of this disturbance on the equivalent Thevenin circuit (as seen from the inverter terminals) is shown in Fig. 4. The disturbance signal virtually creates a kind of second harmonic voltage (due to angle 2θ). The magnitude of this voltage ($\frac{k}{2}\sqrt{2}I_{\mathrm{rms}}Z_{\mathrm{th}}$) should be smaller than 2.5% of the magnitude of the basic frequency ($\sqrt{2}I_{\mathrm{rms}}Z_{\mathrm{th}}$), according to EN 50160 Standard for weak island networks [30]. Therefore, the gain k should take values smaller than or equal to 0.05.

The feedback value of the disturbance can be calculated by a *d-q* PLL [31] through the Park transformation of the d-axis component of the voltage, V_{mgd}, as

$$\begin{bmatrix} V_{\mathrm{mgd}} \\ V_{\mathrm{mgq}} \\ V_{\mathrm{mg0}} \end{bmatrix} = \sqrt{\frac{2}{3}} \times \begin{bmatrix} \cos\theta_{\mathrm{PLL}} & cos(\theta_{\mathrm{PLL}} - \frac{2\pi}{3}) & \cos(\theta_{\mathrm{PLL}} + \frac{2\pi}{3}) \\ \sin\theta_{\mathrm{PLL}} & \sin(\theta_{\mathrm{PLL}} - \frac{2\pi}{3}) & \sin(\theta_{\mathrm{PLL}} + \frac{2\pi}{3}) \\ \frac{\sqrt{2}}{2} & \frac{\sqrt{2}}{2} & \frac{\sqrt{2}}{2} \end{bmatrix} \cdot \begin{bmatrix} V_a \\ V_b \\ V_c \end{bmatrix} \tag{7}$$

$$\begin{bmatrix} V_a \\ V_b \\ V_c \end{bmatrix} = \begin{bmatrix} \sqrt{2}V_{\mathrm{rms}}\sin\theta_c \\ \sqrt{2}V_{\mathrm{rms}}\sin(\theta_c - \frac{2\pi}{3}) \\ \sqrt{2}V_{\mathrm{rms}}\sin(\theta_c + \frac{2\pi}{3}) \end{bmatrix}. \tag{8}$$

By using (7) and (8), the *dq* PLL transforms the three-phase voltages $V_{a,b,c}$ in *dq* reference frame, where V_{mgq} corresponds to the magnitude of the phase voltage and V_{mgd} takes the following form:

$$V_{\mathrm{mgd}} = \sqrt{3}V_{\mathrm{rms}}\sin(\theta_c - \theta_{\mathrm{PLL}}). \tag{9}$$

Assuming that $\theta_c - \theta_{\mathrm{PLL}} \approx 0$, then $\sin(\theta_c - \theta_{\mathrm{PLL}}) \approx \theta_c - \theta_{\mathrm{PLL}}$. As it is presented in Fig. 3(b), the angle θ_{PLL} results from the error of the d-axis component of the voltage V_{mgd}. The following transfer function in Laplace domain is obtained after some mathematical manipulations, taking into account (9) and the aforementioned assumptions:

$$V_{\mathrm{mgd}}(s) = \sqrt{3}V_{\mathrm{rms}}\left(\frac{s^2}{s^2 + K_p\sqrt{3}V_{\mathrm{rms}}s + K_i\sqrt{3}V_{\mathrm{rms}}}\right)\cdot \times \left(\frac{\omega}{s^2} + \frac{k\cdot\omega}{s^2+\omega^2}\right) \tag{10}$$

where $\omega = 2\pi f$, and K_p and K_i are the proportional and integral term of the PI controller. By setting a step change 0.2 p.u. on the magnitude of V_{mgd} and on the response time (less than three cycles), K_p and K_i can be calculated from (10). Therefore, the detection time is also restricted to less than three cycles. During this small time period, the control of the DERs remains in droop control mode but senses a low voltage, which in turn forces the converter to inject large currents. However, under droop control mode, limiters restrict the converter output current, in order to protect the semiconductor switches. Since V_{rms} is proportional to the equivalent Thevenin impedance Z_{th} as in Fig. 4, then according to (9), the rms value of V_{mgd} is also proportional to Z_{th}. The time-domain function of (10) is a sinusoidal signal with frequency equal to the fundamental and magnitude proportional to the impedance. As a result, by measuring the $V_{\mathrm{mgd\,rms}}$ at the fundamental frequency, any relatively large variation in the topology of the microgrid can also be detected. It should be mentioned that $V_{\mathrm{mgd\,rms}}$ is not sensitive to load variations, because Z_{th} is formed by the parallel combination of the line impedances, the fault impedance, and the

equivalent load impedance, with the latter being much larger than the former. Thus, when the measured value drops below a threshold λ_s, a faulty situation is identified and the signal "*fault*" is generated, in order to switch the control strategy from droop control to current control mode. The threshold λ_s can be calculated by (10) by taking into account that a fault corresponds to a voltage $V_{\rm rms} < 80\%$ of the nominal. Node voltages $80\% < V_{\rm rms} < 100\%$ of the nominal can be considered as voltages sags and not faults.

In case of a harmonic polluted voltage, the *d*-axis voltage component is also polluted. However, the fault-detection method is based on the magnitude of the fundamental component of the *d*-axis component, which is derived after filtering. For this reason, the fault-detection method is not affected by harmonics.

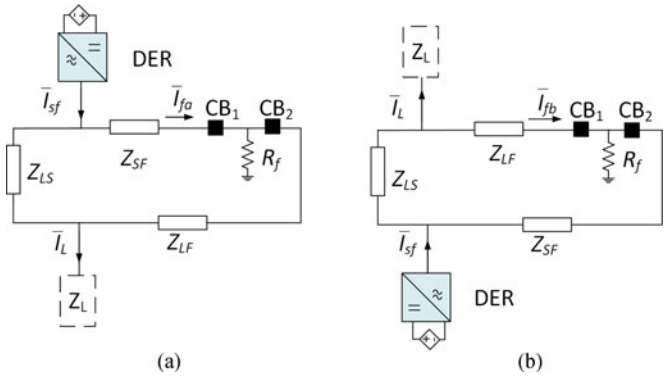

Fig. 5. Source current contribution to the fault.

C. Fault-Protection System Design

When a fault is identified with the aforementioned method, the protection device closer to the fault should be activated first, in order to disconnect only the faulty part. The protection devices can be circuit breakers (CBs) with simple overcurrent tripping, which are triggered by measuring a current larger than the rated one. However, in a converter-dominated islanded microgrid, the injected currents are limited to only a few times the nominal one for protecting the semiconductor switches. Another problem with low-voltage microgrids is the relatively large voltage drops and power losses during the fault due to the large line impedances. During the fault, the RL-type loads still absorb current and a significant active power is needed to cover the increased losses. The situation is even worse in case of a high-impedance fault. Therefore, mainly active power is required during the fault due to the large ohmic losses on the distribution lines and for the remaining active power absorbed by the loads under reduced voltage. The required reactive power is much less than the active one and corresponds to the consumption on the inductive parts of the distribution lines and loads under reduced voltage. In case the available active power from the DERs is not sufficient, an appropriately sized supercapacitor ESS is assumed to be connected in the dc link of each DER. The supercapacitor bank with the dc/dc converter and its respective cost per energy unit are analytically presented in [32], while its cost can be assumed to be of the order of €25/Wh. The sizing of the supercapacitor depends on the nominal power of each DER and the time duration of the fault clearing. In low-voltage grids, the fault is cleared within 1–3 s. The supercapacitor will start discharging in order to keep the dc-link voltage constant if the active power available from the renewable source is not sufficient. Obviously, the discharge current of the supercapacitor ESS is determined by each DER during the fault, as it is explained later, keeping the dc-link voltage constant. Thus, it acts as replacement of the missing renewable active power for the 1–3 s of the fault. In case such an energy storage device is absent, the proposed protection system will not function properly, because the active power needed to feed the fault will not be available, leading to a collapse of the dc voltage of the DERs and, thus, the collapse of the whole microgrid.

Furthermore, it should be mentioned that in low-voltage distribution networks, there might be line faults with currents lower than the rated CB currents. Such faults cause very limited variation in the impedance seen by the DERs, which is similar to the switching of loads. For this reason, the proposed protection method cannot be applied in such cases. Instead, advanced fault-detection devices (e.g., differential current measurement at each branch) and additionally a communication system among the protection devices and the microgrid inverters are necessary.

In case of a line fault within an islanded looped microgrid, the DERs should inject a large enough current, so that 1) the CBs at both ends of the faulty line are activated and 2) the current in these two CBs is larger than the current in the remaining microgrid CBs. Since the load still absorbs current during the fault, this current should be taken into account, when determining the injected by the DERs current. The worst case occurs when the total microgrid load is assumed to be aggregated at just one node. The contribution of each DER is considered separately, taking into consideration the relative position of the DER with respect to the load and the fault, as shown in Fig. 5. In this case, the current that flows through $\rm CB_1$ is calculated by considering two subcases. In the first, presented in Fig. 5(a), the DER is closer to $\rm CB_1$, while in the second [see Fig. 5(b)], the load is closer to $\rm CB_1$. The magnitude of the corresponding fault currents is calculated from (11) and (12)

$$\bar{I}_{\rm fa} = \frac{Z_L(Z_{\rm LF}+Z_{LS})+Z_{LS}(Z_{\rm LF}+R_f)}{Z_{\rm tot}(Z_L+Z_{\rm LF}+R_f)-Z_{\rm LF}^2}\bar{I}_{\rm sf} \quad (11)$$

$$\bar{I}_{\rm fb} = \frac{Z_{\rm SF}Z_L - R_f Z_{LS}}{Z_{\rm tot}(Z_L+Z_{\rm LF}+R_f)-Z_{\rm LF}^2}\bar{I}_{\rm sf} \quad (12)$$

where $\bar{I}_{\rm sf}$ is the injected current by the source, Z_L is the impedance of the aggregated load, $Z_{\rm tot}$ is the aggregated line impedance, $Z_{\rm LF}$ is the impedance among the load and the fault, $Z_{\rm SF}$ is the impedance among the source and the fault, Z_{LS} is the impedance among the load and the source, and R_f is the fault impedance. In general, the aggregated fault current $\bar{I}_f$, assuming that *N* sources contribute to the CB with current $\bar{I}_{\rm fa}$ and *M* sources with $\bar{I}_{\rm fb}$, can be calculated as

$$\bar{I}_f = \sum_{i=1}^{N}\frac{Z_{Li}(Z_{LFi}+Z_{LSi})+Z_{LSi}(Z_{LFi}+R_f)}{Z_{\rm tot}(Z_L+Z_{LFi}+R_f)-Z_{LFi}^2}\bar{I}_{sfi} + \sum_{j=1}^{M}\frac{Z_{SFj}Z_L - R_f Z_{LSj}}{Z_{\rm tot}(Z_L+Z_{LFj}+R_f)-Z_{LFj}^2}\bar{I}_{sfj}. \quad (13)$$

The *rms* value of this current should exceed the rated current of the CB, in order for the CB to be tripped according to the

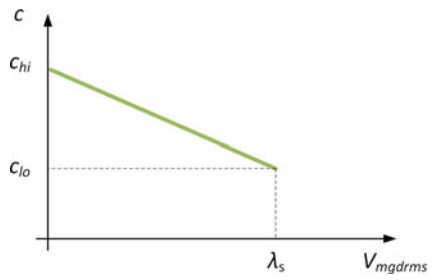

Fig. 6. Droop control curve.

employed overcurrent characteristic. The current injected by each DER during the fault can be calculated by the coefficient c, which indicates the ratio between the fault and the nominal current of each DER

$$I_{sfx} = c \cdot I_{\mathrm{nom}x} \tag{14}$$

where I_{sfx} is the fault current and $I_{\mathrm{nom}x}$ is the normal nominal current of the *x*-DER, respectively. The nominal current of each DER is determined by the nominal active power, power factor, and voltage. The coefficient *c* takes values between c_{lo} and c_{hi}, as it appears in Fig. 6. The lower value c_{lo} is calculated by combining (13) and (14) and considering the current $\left|\bar{I}_f\right|$ equal to the rated current of the CB. It can be proved that one of the worst cases is to consider the fault and the aggregated load close to the node of the DER with the smaller rating. According to this assumption, the several impedances in (13) can also be calculated.

The other important issue is the selective operation of the CBs. Due to the looped topology of the examined microgrid, the current flowing through each CB can have an arbitrary direction and magnitude, as the distribution of the DERs and the loads is also arbitrary. For this reason, each CB should have rated current I_r, which is equal to the aggregation of the nominal currents of all DERs. This rating prevents triggering under normal operation, while allows the operation of the microgrid after the fault clearing and switching of the topology from looped to radial. Therefore, the selectivity of the protection means cannot be achieved by the difference in the rating of the CBs. To tackle with this problem, this paper proposes a new method for controlling the DERs during the fault, so that the selectivity is carried out indirectly by the DERs themselves. The proposed control strategy aims to make the CB closer to the fault sense a larger current than the rest of the CBs. Thus, the DERs closer to the fault should inject relatively larger currents than the ones farther from it. In order to achieve this, each DER injects a current proportional to the measured microgrid impedance, according to a droop curve. In this way, the DER closer to the fault will measure a smaller Z_{th} and will inject a relatively larger current. The measured Thevenin impedance is indirectly measured by the calculated $V_{\mathrm{mgd\,rms}}$. The droop curve is described in (15) and shown in Fig. 6

$$c = c_{\mathrm{hi}} - \beta \cdot V_{\mathrm{mgd\,rms}}. \tag{15}$$

The higher value c_{hi} depends on the short-time maximum current capability of the semiconductor switches of the dc/ac converter. In this paper, the parameter c_{hi} is assumed to be equal to 3. The parameter β is determined by the maximum value of $V_{\mathrm{mgd\,rms}}$ during a high-impedance fault, which corresponds to the threshold λ_s. The following procedure is suggested for determining the slope β of the droop curve:

Step 1: Set the threshold λ_s to the value determined from K_p and K_i in (10) as mentioned above.
Step 2: Assume the entire microgrid load aggregated at the node of the DER with the smaller rating and consider a line fault closer to that DER.
Step 3: Initially set $c_{lo} = c_{\mathrm{hi}} = 3$. The maximum fault impedance R_f can be calculated for I_{f} equal to the smaller tripping current of the CB from (13) and (14).
Step 4: Slightly reduce R_f. A new value for c_{lo} can now be calculated from (13), assuming $c = c_{lo}$ for all DERs in (14).
Step 5: Calculate the currents in all branches by applying the proposed current control method.
Step 6: Check if the currents through the CBs guarantee sufficient time discrimination, which depends on the tolerances of the time–current characteristics of the CBs.
Step 7: If the time discrimination is not sufficient, R_f should be reduced. Repeat steps 4–6.
Step 8: If step 6 is satisfied, the highest impedance fault and the required droop curve have been defined.

It is evident from the aforementioned procedure that both the maximum fault impedance that can be cleared and the resulting droop curve depend on the time–current characteristic of the CBs. Therefore, this procedure should be repeated for every type of time–current characteristic.

The transition from the droop control strategy to current mode can also be seen in Fig. 3(a), which is activated by the signal "*fault.*" When the signal "*fault*" is equal to 0 (steady-state operation), the DER operates in droop control mode. On the other hand, when the DER identifies a fault, signal "*fault*" is set equal to 1 and the DER switches to current control operation mode. In this mode, the references of the currents are calculated according to the proposed algorithm and serve as inputs in the current controller, as shown in Fig. 3(a). The frequency of the injected current during the fault is set equal to the nominal of 50 Hz. In case of a symmetrical fault, the *d*-axis reference current $I_{d\mathrm{ref\_fault}}$ is set equal to I_{sf}, while $I_{q\mathrm{ref\_fault}}$ is set equal to zero.

D. Asymmetrical Fault Control Strategy

The detection of an asymmetrical fault can be implemented with the above presented fault-detection method, by using an orthogonal signal generator second-order generalized integrator (OSG-SOGI) PLL for each phase [33], [34]. The faulty phase is identified by the reduction of the representative indirect measured impedance through the $V_{\mathrm{mgd\,rms},i}$ (for $i = a, b, c$ phase) parameter. The output *d*-axis voltage component of the single-phase PLL is $\sqrt{3}$ smaller than the three-phase PLL; thus, the threshold λ_{as} is $\sqrt{3}$ times smaller, compared to corresponding threshold λ_s of the symmetrical fault. In order to clear the fault, a combination of positive-, negative-, and zero-sequence reference currents is produced. When the measured impedance of a phase is lower than the threshold λ_{as}, the control stores the *rms* value of the currents of the "healthy" phases. In this way, the reference current of the faulty phase is calculated by the coefficient *c*, while the reference current of the other phases takes the stored value. The coefficient *c* is calculated by using (15), where the upper bound of $V_{\mathrm{mgd\,rms},i}$ is replaced by λ_{as}. Therefore,

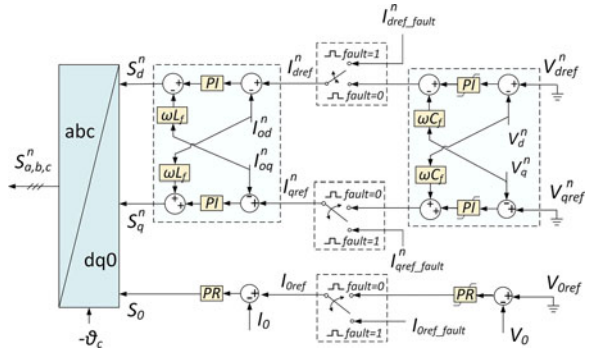

Fig. 7. Negative- and zero-sequence control strategy.

a larger current is injected only in the faulty phase, while the healthy phases continue operating as in the prefault situation. The frequency of the injected currents is again set equal to 50 Hz. The reference positive-, negative-, and zero-sequence currents are calculated according to Park transformation

$$\begin{bmatrix} I_{d\mathrm{ref}} \\ I_{q\mathrm{ref}} \end{bmatrix} = \sqrt{\frac{2}{3}} \begin{bmatrix} \cos(\omega t) & \cos(\omega t - \frac{2\pi}{3}) & \cos(\omega t + \frac{2\pi}{3}) \\ \sin(\omega t) & \sin(\omega t - \frac{2\pi}{3}) & \sin(\omega t - \frac{2\pi}{3}) \end{bmatrix} \cdot \times \begin{bmatrix} I_{a\mathrm{ref}} \\ I_{b\mathrm{ref}} \\ I_{c\mathrm{ref}} \end{bmatrix} \tag{16}$$

$$\begin{bmatrix} I^n_{d\mathrm{ref}} \\ I^n_{q\mathrm{ref}} \\ I_{0\mathrm{ref}} \end{bmatrix} = \sqrt{\frac{2}{3}} \times \begin{bmatrix} \cos(-\omega t) & \cos(-\omega t - \frac{2\pi}{3}) & \cos(-\omega t + \frac{2\pi}{3}) \\ \sin(-\omega t) & \sin(-\omega t - \frac{2\pi}{3}) & \sin(-\omega t + \frac{2\pi}{3}) \\ \frac{\sqrt{2}}{2} & \frac{\sqrt{2}}{2} & \frac{\sqrt{2}}{2} \end{bmatrix} \cdot \begin{bmatrix} I_{a\mathrm{ref}} \\ I_{b\mathrm{ref}} \\ I_{c\mathrm{ref}} \end{bmatrix} \tag{17}$$

where $\omega = 2\pi 50$ [r/s] ; $I_{\mathrm{dref\_fault}}, I_{\mathrm{qref\_fault}}, I^n_{\mathrm{dref\_fault}}$, $I^n_{\mathrm{qref\_fault}}$, and $I_{0\mathrm{ref\_fault}}$ are the positive-, negative-, and zero-sequence reference currents; and $I_{a\mathrm{ref}}, I_{b\mathrm{ref}}$, and $I_{c\mathrm{ref}}$ are the reference currents in the *abc*-rotating system. The control strategy is also shown in Fig. 7. The measured three-phase voltages $V_{a,b.c}$ and currents $I_{oa,ob,oc}$ are transformed into the negative- and zero-sequence quantities, respectively, by means of Park transformation with the negative control angle $-\theta_c$. The zero-sequence control consists of proportional-resonant (PR) controllers, because both the zero-sequence voltage and the current components vary sinusoidally. The negative- and zero-sequence control strategy is also used in normal condition, in order to zero the respective sequence components of the voltage, in case of asymmetrical loads.

The control strategy for both symmetrical and asymmetrical faults is summarized in the flowchart in Fig. 8.

III. Simulation Results

The control strategy is tested in a looped microgrid, consisting of four converter-interfaced DERs with aggregated active power 40 kW and three RL loads, as in Fig. 1. Each converter is assumed to be able to operate also under 0.9 power factor at 400-V line voltage at the ac side. The dc voltage is the same for each DER and equal to 800 V. The switching frequency of the converters equals 9.75 kHz, while the rest parameters of the DERs appear in Table I and the load parameters in Table II. The nominal current of the DERs is calculated from the nominal values of the active power, power factor and voltage.

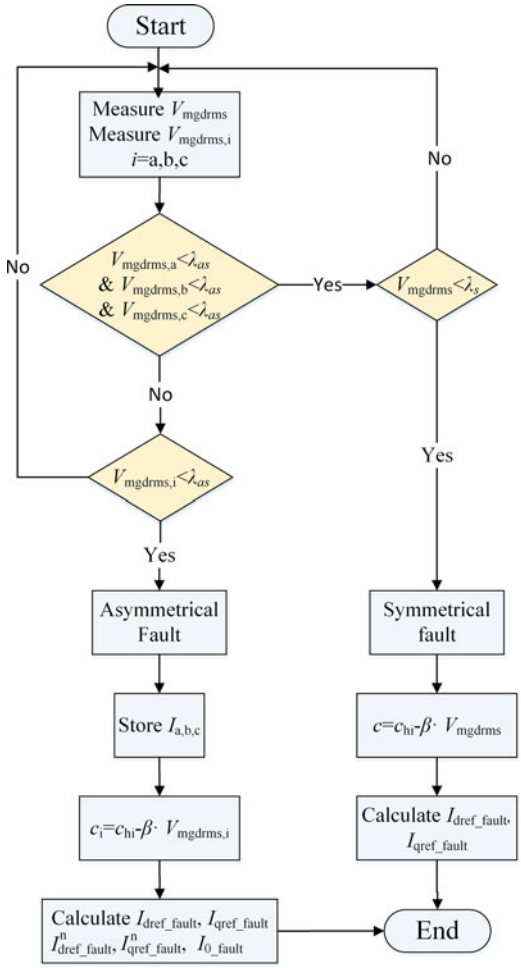

Fig. 8. Control strategy for symmetrical and asymmetrical faults.

TABLE I
System Parameters

Items	DER_1	DER_2	DER_3	DER_4
Nominal line voltage	400 V	400 V	400 V	400 V
Rated power P	10 kW	3 kW	12 kW	15 kW
Nominal power factor	0.9	0.9	0.9	0.9
Nominal current I_{nom}	16.04 A	4.81 A	19.25 A	24.06 A
Filter inductance L_f	2 mH	0.6 mH	2.4 mH	3 mH
Filter capacitance C_f	15 μF	50 μF	12.5 μF	10 μF
Droop coefficient m	2×10^{-4}	6.67×10^{-4}	1.66×10^{-4}	1.33×10^{-4}
Droop coefficient n	3.25×10^{-3}	10.83×10^{-3}	2.7×10^{-3}	2.16×10^{-3}
Coefficients m_d, n_d	10^{-5}	10^{-5}	10^{-5}	10^{-5}
Supercapacitor bank energy	11.2 Wh	3.36 Wh	13.44 Wh	16.8 Wh

TABLE II
ELECTRICAL PARAMETERS OF LOADS

Items	R [Ω]	L [H]	P [W] at nominal voltage	Q [Var] at nominal voltage
Three-phase load L_1	12.307	0.0783	13 000	6 500
Single-phase load L_2	35.267	0.1981	1500	850
Three-phase load L_3	9.143	0.0636	17 500	8000

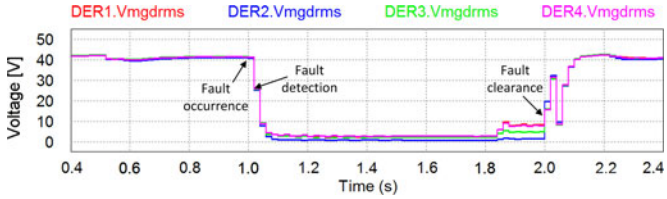

Fig. 9. Feedback d-axis voltage $V_{\mathrm{mgd\,rms}}$ [V] from the PLL.

The parameters of the *LC* filter is selected so that the voltage drop across L_f is <1% with nominal current and $\mathrm{THD_V}$ <5%. The distribution lines within the microgrid are assumed to be overhead ACSR 16-mm^2 electrical lines with $R = 1.268\ \Omega$/km and $X = 0.422\ \Omega$/km. The lengths of the respective connection lines are $L_{\mathrm{line1}} = 400$ m, $L_{\mathrm{line2}} = L_{\mathrm{line3}} = L_{\mathrm{line4}} = 100$ m, $L_{\mathrm{line5}} = 200$ m, and $L_{\mathrm{line6}} = 50$ m. The line CBs are assumed to be equipped with extremely inverse time–current characteristics. The time–current equation of each CB is described by

$$t = 0.03 \cdot \left[\frac{28.2}{(I_f/I_r)^2 - 1} + 0.1217\right], \quad \text{for } 1.1 \cdot I_r < I_f < 3 \cdot I_r \tag{18}$$

where t is the trigger time and I_r is the rated of the CB [24]. In this case, the rated current equals to 64.15 A for $S_{\mathrm{total}} =$ 40 kVA. The maximum fault duration $t_{\max}$ for $I_f = 1.1 \cdot I_r$, according to (18) is 4.032 s. For this time duration, the supercapacitor energy bank for each DER can be calculated ($P_{\mathrm{nom}} \cdot t_{\max}$), as it is presented in Table I. Generally, it can be said that the introduction of the supercapacitor ESS will add approximately 10% in the cost, volume, and weight [35] of the dc/ac converter.

Alternatively, CBs equipped with S-type characteristics can be used. Since the nominal current is calculated to 64.15 A, a CB equipped with current sensor similar to ABB PR 222 DS/P [25] with nominal current $I_n = 100$ A can be implemented. The S-characteristic is adjusted to $I_2 = 0.65 \cdot I_n = 65$ A and the time response is adjusted to 0.05 s (it is an option given by the CB manufacturer). The quantity of I^2t is calculated by considering eight times the nominal current I_n (this is defined by the CB manufacturer); thus

$$I^2t = (8 \cdot I_n)^2 t = (8 \cdot 100)^2 \cdot 0.05 = 32,000[\mathrm{A}^2 \cdot \mathrm{s}]. \tag{19}$$

The tripping time of this CB is calculated by dividing the quantity I^2t of (19) with the square of the fault current that flows through the CB.

The proportional and integral parameters of the PI controller of the PLL are calculated from (10) to be $K_p = 0.3$ and $K_i = 300$ by setting the following constraints: $V_{\mathrm{mgd\,rms}} = \lambda_s =$ 32.5 V (i.e., 10% of the peak value of the nominal phase voltage), while the time response for a 0.2-p.u. step change of V_{rms} (step change from the nominal voltage to 80% of the nominal, which

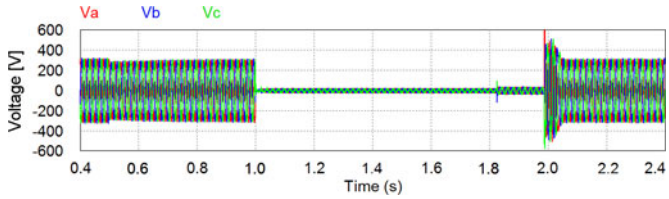

Fig. 10. Three-phase voltage profile [V] at the point of connection of load.

TABLE III
RMS VALUE OF DER CURRENTS [A] IN PHASE A

t [s]	$\mathbf{DER_1}$	$\mathbf{DER_2}$	$\mathbf{DER_3}$	$\mathbf{DER_4}$
1.02–1.826	46.34 (2.89 p.u.)	14.36 (2.99 p.u.)	55.74 (2.89 p.u.)	69.14 (2.87 p.u.)
1.826–1.988	44.01 (2.74 p.u.)	14.32 (2.98 p.u.)	54.78 (2.84 p.u.)	66.16 (2.75 p.u.)

can be perceived as fault) is set equal to three cycles of 50 Hz. This is the minimum response time to calculate in a reliable way the $V_{\mathrm{mgd\,rms}}$, since the calculation of the rms value takes at least one cycle. The corresponding threshold for an asymmetrical fault is $\lambda_{as} = 18.76$V. Following the procedure mentioned in Section II-C, in order to achieve the necessary fault current for tripping the CBs and obtain the time discrimination for the examined microgrid, a high-impedance fault is calculated as the one corresponding to short-circuit power equal to eight times the nominal aggregated active power of the DERs, i.e., 8·40 kW = 320 kW; thus, $R_f = 0.5\ \Omega$. The lower value of the parameter c_{lo} is calculated by assuming that the aggregated nominal load is connected at the node of the smaller DER, i.e., at $\mathrm{DER_2}$. The fault takes place in Line 1. The distance between $\mathrm{CB_1}$ and the fault is 100 m, while between $\mathrm{CB_2}$ and the fault is 300 m. From (13), the currents at both ends of the line are 31 A for $\mathrm{CB_1}$ and 29.63 A for CB2. Therefore, the parameter c_{lo} can be calculated by dividing the rated current with the current of $\mathrm{CB_1}$, i.e., it is equal to 2.07. Thus, $\beta = 0.0283$, and consequently, the resulting droop curve is $c = 3 - 0.0283 \cdot V_{\mathrm{mgd\,rms}}$. The simulation tests are conducted with PSIM Software.

A. Solid Three-Phase Fault

At the beginning of the first simulation test, the microgrid operates without the three-phase load L_1, which is connected at $t = 0.5$ s. The impact of the sudden load connection appears as voltage sag (see Fig. 10), while the feedback $V_{\mathrm{mgd\,rms}}$ has a small transient effect. The voltage component $V_{\mathrm{mgd\,rms}}$ is not reduced below the lower threshold, as it is presented from Fig. 9. Thus, with the proper selection of threshold λ_s, even large load variations can be correctly detected as such and not as faults. In case of a load disconnection, which leads to a voltage swell, the microgrid impedance increases. Therefore, it cannot be perceived as a fault. Subsequently, at $t = 1$ s, a three-phase solid fault takes place. The equivalent fault impedance is $R_f = 0.001$ Ω. In the prefault condition, the DERs operate according to their droop coefficients. The fault is identified at $t = 1.02$s, because $V_{\mathrm{mgd\,rms}} < \lambda_s$, as it is illustrated in Fig. 9. The fault-detection time can be considered as quite small, compared with other fault-detection methods, where is calculated as a few cycles

TABLE IV
RMS VALUE OF CURRENTS [A] AT SOLID THREE-PHASE FAULT WITH THE PROPOSED CONTROL STRATEGY AND TRIPPING TIME WITH CBS EQUIPPED WITH EXTREMELY INVERSE-TIME CURVE (18) OR WITH I^2t RELEASE[1]

Row		CB_1	CB_2	$CB_{3\&4}$	$CB_{5\&6}$	$CB_{7\&8}$	$CB_{9\&10}$	$CB_{11\&12}$
1	Current [A] at $t = 1.1$s	91.37	90.26	76.18	77.46	78.25	21.83	42.73
2	Trip time [s] with (18)	0.826	0.867	2.066	1.85	1.737	-	-
3	Δt [ms]	-	41	1240	1024	911	-	-
4	Trip time [s] with I^2t	3.833	3.928	5.514	5.333	5.226	-	-
5	Δt [ms]	-	95	1,681	1,500	1,393	-	-
6	Current [A] at $t = 1.9$ s	0	161.64	147.9	150.15	151.61	97	43.67
7	Trip time [s] with (18)	-	0.162	0.200	0.193	0.188	0.661	-
8	Δt [ms]	-	-	37.7	31	26	499.3	-
9	Trip time [s] with I^2t	-	0.030	0.446	0.399	0.371	3.4	-
10	Δt [ms]	-	-	416	369	341	3,370	-

[1] Δt: time discrimination between a CB and the tripped one, Trip time: the time it takes a CB to trip after sensing a certain current.

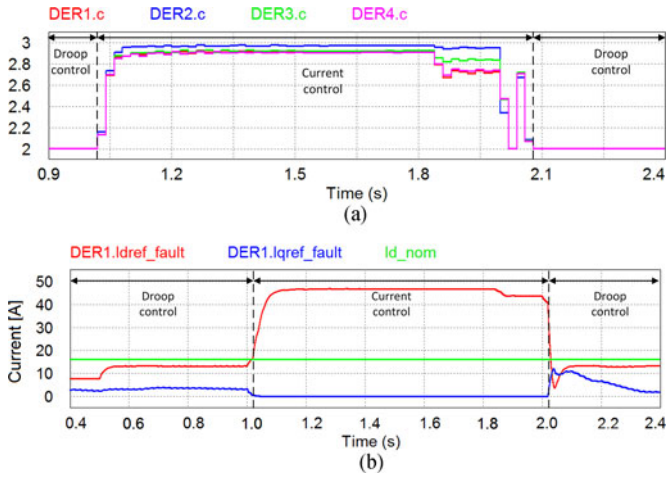

Fig. 11. (a) Parameter c of the proposed droop curve. (b) Reference currents $I_{d\mathrm{ref}}$ and $I_{q\mathrm{ref}}$ of current control of DER_1. With I_{nom} is denoted the nominal current of DER_1.

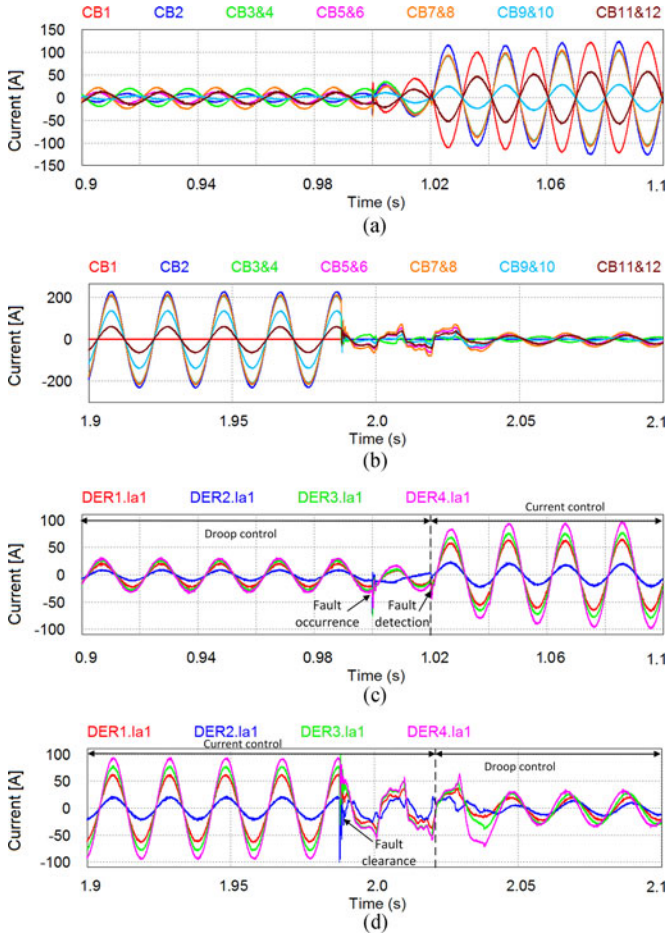

Fig. 12. (a) Current [A] through the CBs at the transition from normal to fault operation. (b) Current [A] through the CBs at the transition from fault to normal operation. (c) Output current [A] of phase a of each DER at the transition from normal to fault operation. (d) Output current [A] of phase a of each DER at the transition from fault to normal operation.

(e.g., 15 cycles in [19]). During the fault, the *rms* value of CB_1 is 91.37 A, which is larger than the rated current, and consequently, it is triggered at $t = 1.826$s, i.e., the response time of this CB is 0.806 s. After the trigger of CB_1, the fault current that flows through CB_2 becomes 161.64 A, and finally, it trips at $t = 1.988$ s (i.e., 162 ms after the triggering of CB_1), isolating the faulty segment of the microgrid. The triggering time of each CB can be verified by (18). Thus, CB_1 and CB_2 are correctly tripped first, as being closer to the fault. This proves that the selectivity coordination is carried out by the injected currents from the DERs. The *rms* values of the output currents of phase *a* of each DER are presented in Table III (the per unit values are also given in parenthesis), while the respective *rms* values of the CBs are listed in Table IV. Table IV also presents the tripping time of CBs adopting the extremely inverse time curve of (18) (rows 2 and 7) and the alternative type of I^2t characteristic (rows 4 and 9). It is obvious from Table IV that the selectivity is ensured, first for CB_1 and then for CB_2, while the respective time difference is larger in case of using CBs equipped with I^2t release. Furthermore, the tripping time is larger in case of implementing CBs equipped with I^2t release, requiring larger supercapacitors. The instantaneous current waveforms are illustrated in Fig. 12. From these figures, it can be noticed that the DERs switch from droop control to current control mode in approximately one period of the fundamental frequency, increasing the injected currents to c times the nominal ones. The parameter c is different for each individual DER [see Fig. 11(a)], since it depends on the location of the DER with respect to the location of the fault. It can be deduced that the desired selectivity is achieved successfully.

When the fault is cleared, the microgrid voltage returns to the steady-state operation. The control of the DERs remains in current control mode, until parameter $V_{\mathrm{mgd\,rms}}$ surpasses the λ_s threshold at $t = 2.03$ s, as shown in Fig. 9. Thus, at this moment, the DERs switch to droop control again (see Fig. 11), which is reflected in new steady-state currents, as illustrated in Fig. 12(d). The variation of the reference currents $I_{d\mathrm{ref}}$ and $I_{q\mathrm{ref}}$ of DER_1 during the simulation test can be seen in Fig. 11(b). When DER_1 operates in droop control mode, the reference currents are calculated from the output of the voltage controller. During the fault, the DER control switches from droop to current control

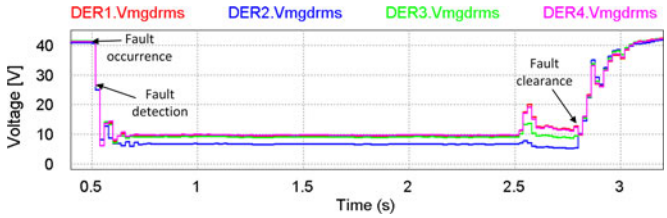

Fig. 13. Feedback d-axis voltage $V_{\mathrm{mgd\,rms}}$ [V] from the PLL.

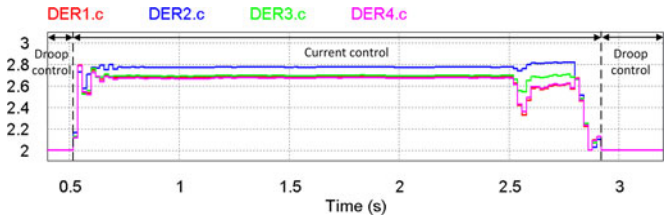

Fig. 14. Parameter c of the proposed droop curve.

TABLE V
RMS VALUE OF CURRENTS [A] AT HIGH-IMPEDANCE FAULT WITH THE PROPOSED CONTROL STRATEGY

t [s]	CB_1	CB_2	$CB_{3\&4}$	$CB_{5\&6}$	$CB_{7\&8}$	$CB_{9\&10}$	$CB_{11\&12}$
0.6	**76.62**	71.74	58.20	66.24	69.29	17.34	32.48
2.7	0	**131.63**	101.72	108.93	111.85	60.98	18.89

mode, injecting a current $I_{d\mathrm{ref}}$, which is c times the nominal current I_{nom}, while $I_{q\mathrm{ref}}$ is set to zero. When the fault is cleared, the DER returns to droop control, while the reference currents return to the respective values of the prefault operation.

B. High-Impedance Three-Phase Fault

In this simulation case, the fault impedance is $R_f = 0.5\ \Omega$. The fault takes place at $t = 0.5$ s. The difference between a solid and a high-impedance fault is reflected in the variation of the parameter c, which determines the injected currents during the fault. The discretization is better in case of a high-impedance fault, as the measured microgrid impedance is larger for all DERs. The feedback voltage $V_{\mathrm{mgd\,rms}}$ and the respective impact on the parameter c are illustrated in Figs. 13 and 14. In this test, the current of CB_1 becomes equal to 76.62 A, causing its tripping at $t = 2.5$ s. Subsequently, the current of CB_2 becomes equal to 142.94 A, causing its tripping at $t = 2.76$ s. The *rms* value of the currents at each CB appears in Table V.

In order to show the effectiveness of the proposed method for implementing the selectivity with the simple overcurrent CBs, the same simulation is carried out, but now coefficient c is set equal to 3 for all DERs. The *rms* values of each CB current are presented in Table VI. First, CB_1 is correctly activated. However, consequently, the current through $CB_{7\&8}$ is the larger one, activating them incorrectly and isolating the microgrid segment that includes the two loads and the DER_2.

C. High-Impedance Phase-to-Ground Fault

The final case concerns a high-impedance phase a-to-ground fault. In simulation terms, the fault resistance R_f is equal to

TABLE VI
RMS VALUE OF CURRENTS [A] AT HIGH-IMPEDANCE FAULT WITH CURRENT COEFFICIENT $c = 3$

t [s]	CB_1	CB_2	$CB_{3\&4}$	$CB_{5\&6}$	$CB_{7\&8}$	$CB_{9\&10}$	$CB_{11\&12}$
0.6	**115.11**	48.45	33.92	42.84	46.08	11.13	67.55
2.7	0	151.71	137.05	148.45	**152.95**	94.91	47.85

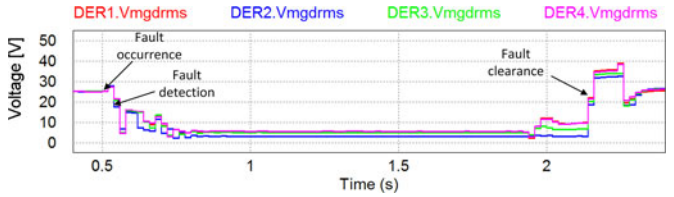

Fig. 15. Feedback d-axis voltage $V_{\mathrm{mgd\,rms}}$ [V] from the OSG-SOGI PLL of phase A.

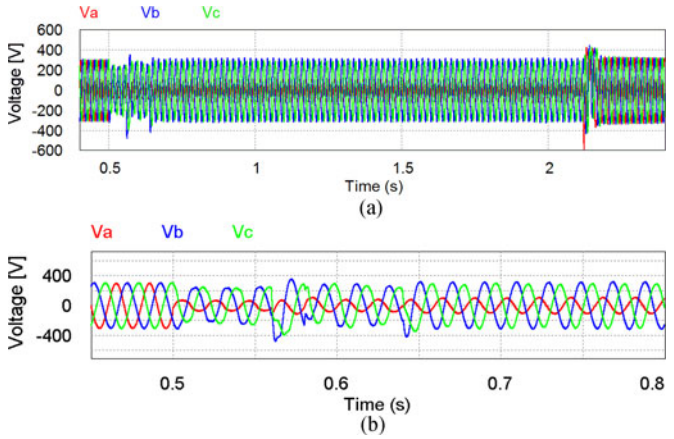

Fig. 16. Three-phase voltage profile [V] at the point of connection of load L_1: (a) during all the simulation time period and (b) during the fault-detection.

0.35 Ω and the fault occurs at $t = 0.5$ s. The objective during an asymmetrical fault is that the healthy phases should remain unaffected. The fault-detection parameter $V_{\mathrm{mgd\,rms}}$, as it is measured by the OSG-SOGI PLL of the voltage of phase a, appears in Fig. 15. At $t = 1.913$ s, the CB_1 of phase a trips, while at $t = 2.123$ s, CB_2 of phase a trips too, isolating the fault. The overcurrent sensors of the healthy phases do not sense any fault, because their currents continue to be as in the prefault condition.

The three-phase voltage at the point of connection of load L_1 is presented in Fig. 16. The voltage of the faulty phase a decreases during the fault, while the healthy phases remain unaffected by the fault. Furthermore, after the fault clearance, the voltage recovers very quickly, with a seamless transient. The parameters c of the currents are shown in Fig. 17(a), while Table VII indicates the *rms* value of phase a currents through each CB. It is evident that proper selectivity has been achieved for asymmetrical faults, too. Fig. 17(b)–(e) presents the DER phase currents. The current of the faulty phase a is increased when the fault is identified, while the currents of the healthy phases remain unaffected after a short transient. Furthermore, it can be noticed that the control system detects the fault after approximately three cycles, while there is a transient period of

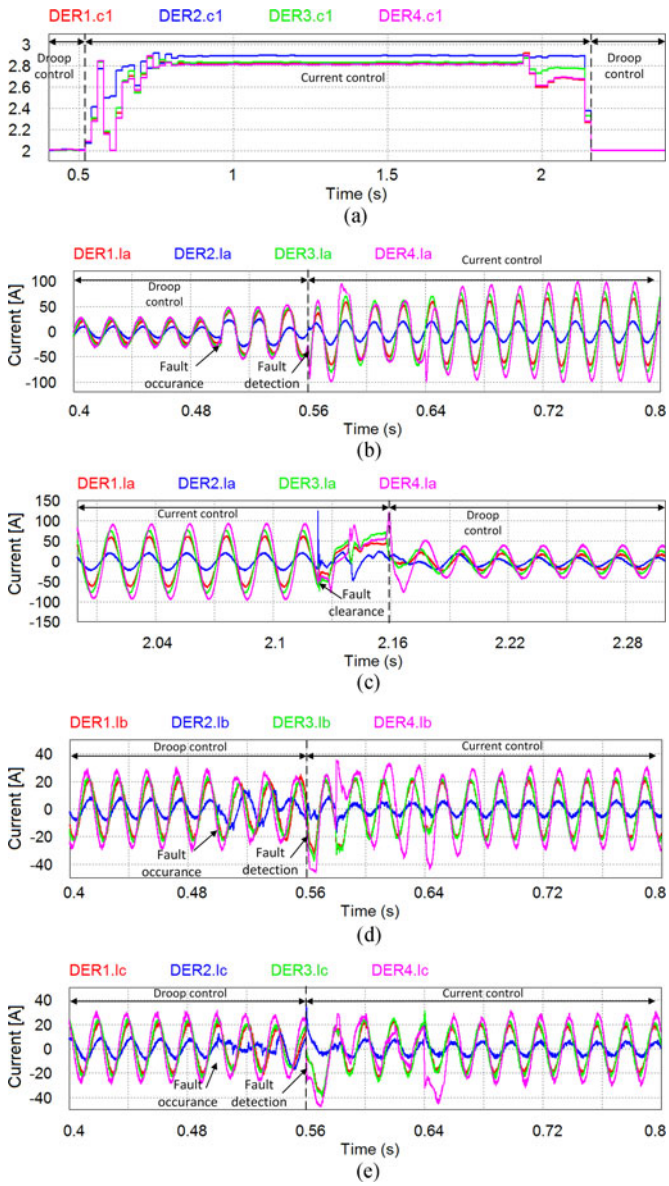

Fig. 17. (a) Parameter c of the proposed droop curve. Output phase current of all DERs. (b) Current of phase a at the transition from normal to fault operation. (c) Current of phase a at the transition from fault to normal operation. (d) Current of phase b at the transition from normal to fault operation. (e) Current of phase c at the transition from normal to fault operation.

about four cycles to inject the faulty current. The currents of the healthy phases are only slightly affected during this transition period [see Fig. 17(d) and (e)]. After the fault clearing, the transition from the current control to the droop control is similar to the one presented for the three-phase fault.

IV. Experimental Results

An experimental validation of the proposed control strategy is carried out in a microgrid with two DERs of nominal capacity 500 W each, having as a primary source ten batteries Bosch D126 of 12-V nominal dc voltage (120 V in total). The *rms* value of the ac line voltage, produced by the PWM control strategy, equals to 73.48 V/50 Hz. The *LC* filter parameters are 0.35 mH and 85 μF. The DERs are connected in looped topology

TABLE VII
RMS Value of Currents [A] at High-Impedance Phase-to-Ground Fault

t [s]	CB_1	CB_2	$CB_{3\&4}$	$CB_{5\&6}$	$CB_{7\&8}$	$CB_{9\&10}$	$CB_{11\&12}$
0.6	**76.83**	74.22	60.1	67.55	70.56	18.66	32.25
2.1	0	**149.39**	135.17	143.71	147.42	92.77	46.52

with an *RL* load with parameters $R = 12\ \Omega$ and $L = 80$ mH. The DERs are connected with ac low-voltage cable five-core J1 VV 2.5 mm^2. The distances among the DERs and the load appear in Fig. 18(a). Two CBs with S-type releases of type ABB XT2 Ekip LSI 10 A [25] are placed on the two sides of the line fault.

Each DER uses a dSPACE DS1104 controller board for the implementation of the control systems. Each controller houses the droop control and the fault-detection control. The electrical parameters of the results are measured with a Fluke 434 instrument by using the transient operation and are collected in the respective graphics by means of Fluke Power Quality Analyzer. In the results, the selection X10 is activated, which corresponds to ten periods per graphic. Due to the lack of many probes, the same experiment is repeated several times in order to collect all the data. According to the procedure mentioned earlier, parameters K_p and K_i of the fault-detection control are calculated to be equal to 2 and 2000, respectively, by setting λ_s equal to 6 and $\lambda_{as} = 3.46$. The proportional and integral parameters of the PI controllers are: 0.3 and 1.5 for the positive sequence voltage controller and 0.1 and 20 for the current controller. The negative sequence control is deactivated, because the microgrid operates with a symmetrical load. Finally, the droop coefficients are $m = 4 \times 10^{-3}$ and $n = 0.012$. The droop curve, as described in (15), was set for both DERs equal to $c = 3 - 0.275 \cdot V_{\mathrm{mgd\,rms}}$. The constant term and the slope of the droop curve are precalculated, according to the procedure mentioned in Section II for the specific microgrid.

A. Three-Phase Symmetrical Fault

In the first experiment, a three-phase symmetrical fault takes place between the two DERs, closer to DER_2. Fig. 18 illustrates the experimental microgrid scheme and the corresponding results. The short-circuit is implemented by a switch connected to the ground through a resistance equal to 0.1 Ω. According to Fig. 18(b), the current at branch L_2 becomes larger than the others, leading to the tripping of CB_2 [see Fig. 18(c)]. After a few seconds, the CB_1 is triggered and the fault is cleared [see Fig. 18(d)]. When the fault is detected, DER_2 injects a larger current, as being closer to the fault. However, this situation is inversed when CB_2 is activated, and as a result, DER_1 becomes closer to the fault [see Fig. 18(e)]. In this way, a selective cooperation of the CBs is successfully achieved.

B. Two-Phase to Ground Fault

In the second experiment, a two-phase to ground fault is investigated. Phases a and b participate in the short-circuit. The microgrid under test is illustrated in Fig. 18(a) (denoted as exp. 2), while the results are presented in Fig. 19. When the fault takes place, the voltage at the faulty phases suddenly drop, while the

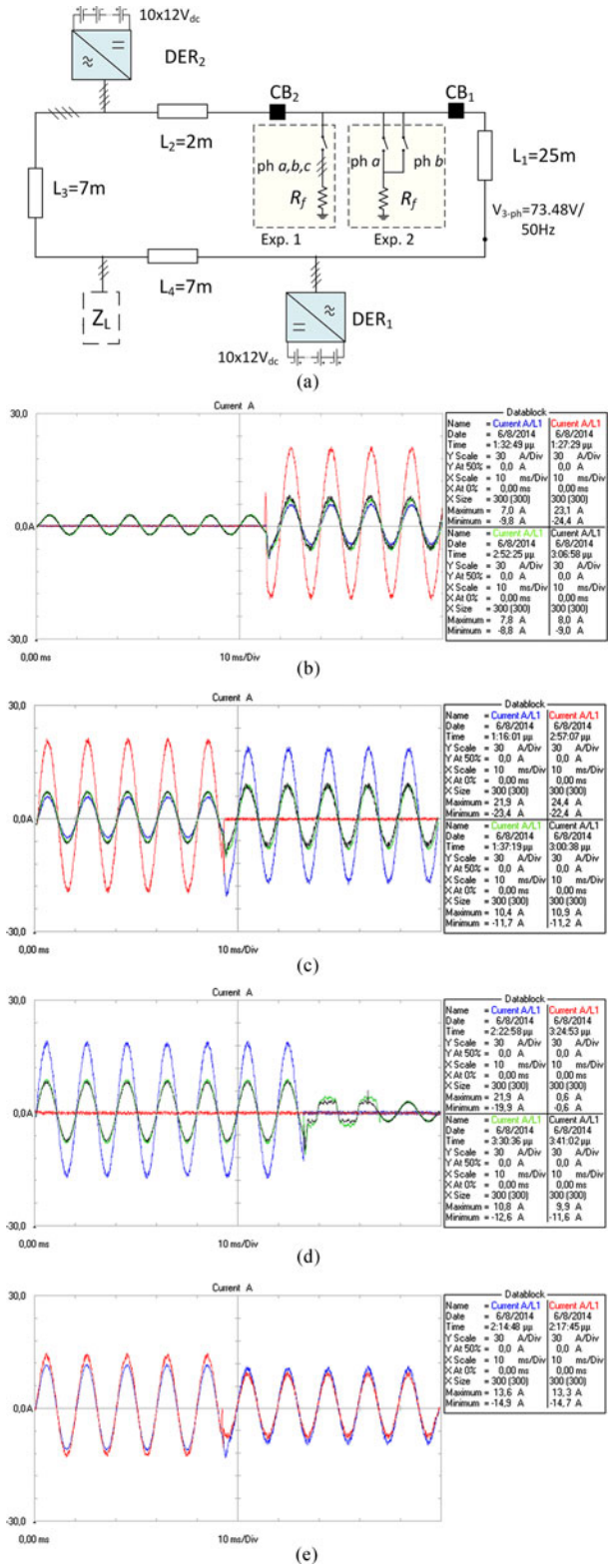

Fig. 18. (a) Experimental microgrid scheme, where Exp. 1 and Exp. 2 correspond to the first and the second experimental test, respectively. (b) Branch currents [A] at the transition from normal to fault operation, (c) at tripping of CB_2, and (d) at tripping of CB_1 and transition back to normal operation (blue line: branch L_1, red line: branch L_2, green line: branch L_3, black line: branch L_4). (e) Output current [A] of each DER during fault (blue line: DER_1, red line: DER_2.

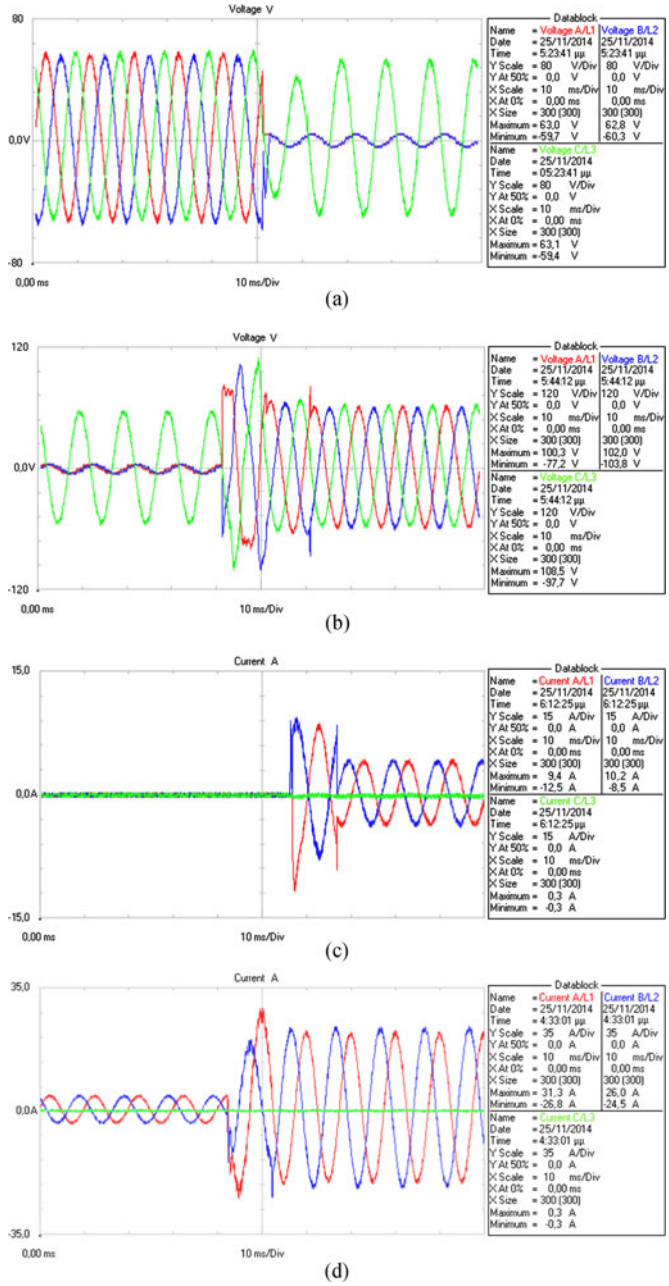

Fig. 19. (a) Phase voltages [V] measured at the load at the transition from normal to fault operation, (b) at the transition back to normal operation (red line: phase a, blue line: phase b, green line: phase c). (c) Phase currents [A] at branch L_1 at the transition from normal to fault operation, (d) at the triggering of CB_2 (red line: phase a, blue line: phase b, green line: phase c).

voltage at the healthy phase c remains almost as in the prefault condition. In Fig. 19(a) and (b) appear the phase voltages at the load during the transition from the normal operation to the faulty and vice versa. The line currents in branch L_1 are illustrated in Fig. 19(c) and (d). In the prefault operation, all branch-L_1 currents are equal to zero due to the topology shown in Fig. 18(a) and due to the fact that the two DERs are of the same rating. Thus, the circulating current among the DERs is zeroed. During the fault, the current of phase c is kept to zero, while the currents of the faulty phases take a larger value, after a short transient [see Fig. 19(c)]. The triggering of the CBs takes place,

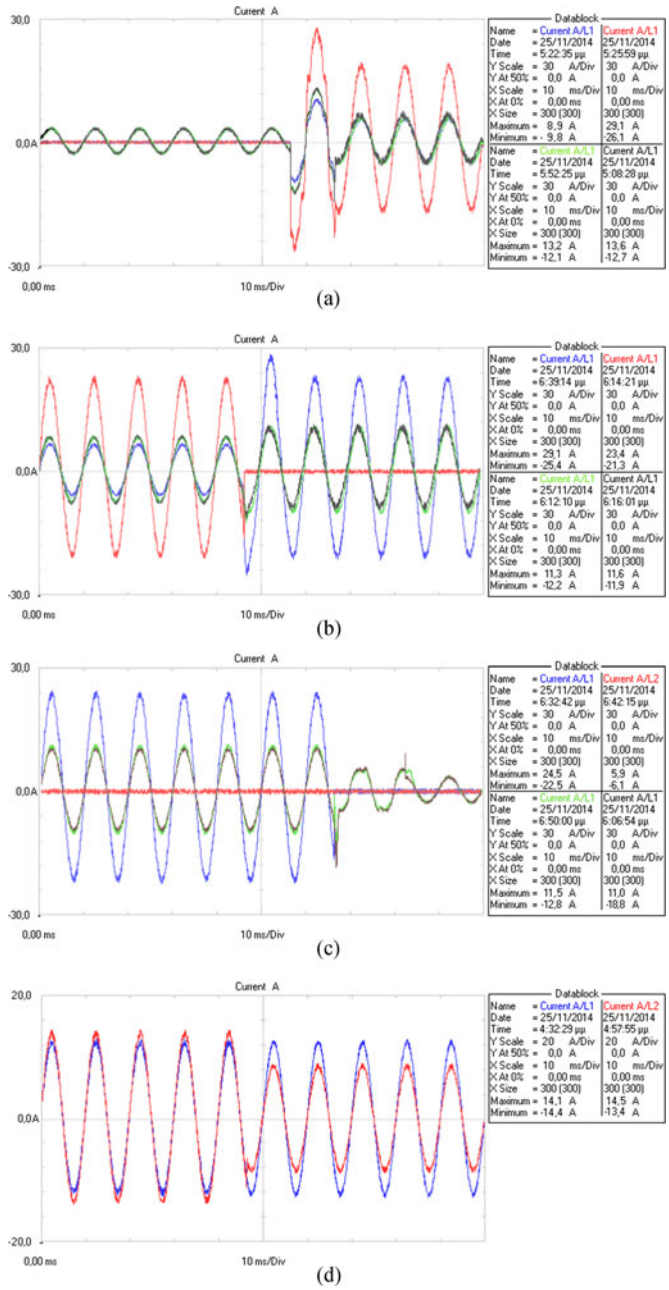

Fig. 20. (a) Branch currents [A] at the transition from normal to fault operation, (b) at tripping of CB_2, (c) at tripping of CB_1 and transition back to normal operation (blue line: branch L_1, red line: branch L_2, green line: branch L_3, black line: branch L_4). (d) Output current [A] of each DER during fault (blue line: DER_1, red line: DER_2).

as in Section IV-A. First, the two poles of CB_2 (corresponding to phases *a* and *b*) are activated, as the current of branch L_2 is relatively larger than the current of branch L_1. Subsequently, the respective two poles of CB_1 are triggered, and finally, the fault is cleared. Fig. 20(a)–(c) shows the current of phase *a* in all branches, while Fig. 20(d) presents the current injections of the two DERs. It is evident that, with the proposed method, the healthy phase remains unaffected and the required overcurrents to achieve selective protection are focused only on the faulty phases.

V. Discussion and Conclusion

A method to tackle with symmetrical and asymmetrical line faults in a looped converter-interfaced microgrid is presented in this paper. By implementing the proposed method, selectivity in the operation of the line protection means can be achieved. All the CBs are assumed to employ simple overcurrent devices with time-inverse current characteristics, without any kind of physical communication among them. Due to the looped topology, each CB has the same rating. When a fault takes place within the microgrid, the control strategy detects the kind of fault in few cycles and changes its inner control from droop to current control. Each converter contributes to the fault with a current, proportional to the indirect measurement of the microgrid impedance, according to a proposed droop curve. In this way, the DER closer to the fault injects a relatively larger current, creating a selectivity, which is absent otherwise. An analytical method for deriving the parameters of the droop curve is also provided. The proposed method is effective for solid and high-impedance (up to a level) three-phase and asymmetrical faults. In the case of asymmetrical faults, the healthy phases remain unaffected. In all cases, the microgrid returns back to normal operation after the fault clearing with a seamless transient effect, although its topology has changed from looped to radial.

The proposed method has the following limitations:

1) The maximum high-impedance fault that can be cleared should be evaluated for each individual looped microgrid like the one mentioned in the paper, taking into account the constraints in the injection of overcurrents by the DERs, the power of the DERs and also the load and the line impedances. The procedure for making such evaluations is presented in the paper.
2) If CBs with inverse time characteristics are used, the time discrimination might be too short. Alternatively, CBs with S-type characteristic (I^2t release) can be used, since they significantly improve the time discrimination. However, since the use of S-type characteristics leads normally to longer fault clearing times, larger supercapacitors ESS will be required. The procedure to evaluate their size and cost is presented in the paper.

The results are validated in a laboratory lower scale microgrid for symmetrical and asymmetrical faults.

References

[1] M. Fotuhi-Firuzabad, R. Iravani, F. Aminifar, N. Hatziargyriou, and M. Lehtonen, "Guest editorial special section on microgrids," *IEEE Trans. Smart Grid*, vol. 3, no. 4, pp. 1857–1859, Dec. 2012.
[2] J. Rocabert, A. Luna, F. Blaabjerg, and P. Rodríguez, "Control of power converters in AC microgrids," *IEEE Trans. Power Electron.*, vol. 27, no. 11, pp. 4734–4749, Nov. 2012.
[3] H. J. Laaksonen, "Protection principles for future microgrids," *IEEE Trans. Power Electron.*, vol. 25, no. 12, pp. 2910–2918, Dec. 2010.
[4] Y. A-R. I. Mohamed and E. F. El-Saadany, "Adaptive decentralized droop controller to preserve power sharing stability of paralleled inverters in distributed generation microgrids," *IEEE Trans. Power Electron.*, vol. 23, no. 6, pp. 2806–2816, Nov. 2008.
[5] K. Oureilidis and C. Demoulias, "An enhanced role for an energy storage system in a microgrid with converter-interfaced sources," *IET J. Eng.*, 2014, Open-access.
[6] P. Nuutinen, P. Peltoniemi, and P. Silventoinen, "Short-circuit protection in a converter-fed low-voltage distribution network," *IEEE Trans. Power Electron.*, vol. 28, no. 4, pp. 1587–1597, Apr. 2013.
[7] N. Nimpitiwan, G. T. Heydt, R. Ayyanar, and S. Suryanarayanan, "Fault current contribution from synchronous machine and inverter based dis-

tributed generators," *IEEE Trans. Power Del.*, vol. 22, no. 1, pp. 634–641, Jan. 2007.
[8] T. Ghanbari and E. Farjah, "Unidirectional fault current limiter: An efficient interface between the microgrid and main network," *IEEE Trans. Power Syst.*, vol. 28, no. 2, pp. 1591–1598, May 2013.
[9] T. Loix, T. Wijnhoven, and G. Deconinck, "Protection of microgrids with a high penetration of inverter-coupled energy sources," in *Proc. CIGRE/IEEE PES Joint Symp. Integr. Wide-Scale Renewable Resources Power Del. Syst.*, 2009, pp. 1–6.
[10] B. Li, Y. Li, Z. Bo, and A. Klimek, "Design of protection and control scheme for microgrid systems," in *Proc. IEEE 44th Int. Universities Power Eng. Conf.*, 2009, pp. 1–5.
[11] H. Wan, K. K. Li, and K. P. Wong, "An adaptive multiagent approach to protection relay coordination with distributed generators in industrial power distribution system," *IEEE Trans. Ind. Appl.*, vol. 46, no. 5, pp. 2118–2124, Sep. 2010.
[12] S. M. Brahma and A. A Girgis, "Development of adaptive protection scheme for distribution systems with high penetration of distributed generation," *IEEE Trans. Power Del.*, vol. 19, no. 1, pp. 56–63, Jan. 2004.
[13] T. S. Ustun, C. Ozansoy, and A. Ustun, "Fault current coefficient and time delay assignment for microgrid protection system with central protection unit," *IEEE Trans. Power Syst.*, vol. 28, no. 2, pp. 598–606, May. 2013.
[14] M. Dewadasa, A. Ghosh, and G. Ledwich, "Protection of microgrids using differential relays," in *Proc. 21st Australasian Univ. Power Eng. Conf.*, 2011, pp. 1–6.
[15] E. Sortomme, S. S. Venkata, and J. Mitra, "Microgrid protection using communication-assisted digital relays," *IEEE Trans. Power Del.*, vol. 25, no. 4, pp. 2789–2796, Oct. 2010.
[16] R. J. Best, D. J. Morrow, and P. A. Crossley, "Communication assisted protection selectivity for reconfigurable and islanded power networks," in *Proc. IEEE 44th Int. Univ. Power Eng. Conf.*, 2012, pp. 1–5.
[17] S. Mirsaeidi, D. M. Said, M. W. Mustafa, M. H. Habibuddin, and Kimia Ghaffari, "An analytical literature review of the available techniques for the protection of micro-grids," *Int. J. Elect. Power Energy Syst.*, vol. 58, pp. 300–306, Jun. 2014.
[18] R. M. Tumilty, M. Brucoli, G. M. Burt, and T. C. Green, "Approaches to network protection for inverter dominated electrical distribution systems," in *Proc. 3rd IET Int. Conf. Power Electron., Mach. Drives*, 2006, pp. 622–626.
[19] M. A. Zamani, T. S. Sidhu, and A. Yazdani, "A protection strategy and microprocessor-based relay for low-voltage microgrids," *IEEE Trans. Power Del.*, vol. 26, no. 3, pp. 1873–1883, Jul. 2011.
[20] M. Dewadasa, R. Majumder, A. Ghosh, and G. Ledwich, "Control and protection of a microgrid with converter interfaced micro sources," in *Proc. Int. Conf. Power Syst.*, 2009, pp. 1–6.
[21] S. A. Saleh, "Signature-coordinated digital multirelay protection for microgrid systems," *IEEE Trans. Power Electron.*, vol. 29, no. 9, pp. 4614–4623, Sep. 2014.
[22] F. Van Overbeeke, "Fault current source to ensure the fault level in inverter-dominated networks," in *Proc. 20th Int. Conf. Exhib. Elect. Distrib.*, 2009, pp. 1–4.
[23] A. Oudalov, A. Fidigatti, T. Degner, B. Valov, C. Hardt, and J. Yarza, "Novel protection systems for microgrids," TC2 Tech. Requirements Netw. Protection, Contract No. SES6-019864, 2009.
[24] *IEEE Standard Inverse-Time Characteristic Equations Overcurrent Relays*, IEEE Std C37112-1996, 1997.
[25] *Low Voltage Molded Case Circuit Breakers up to 1200A*. (2008). Technical catalog. [Online]. Available: http://www.abb.com/
[26] (2011, Sep.). *SACE Tmax XT New Low Voltage Moulded-Case Circuit-Breakers up to 250 A*. [Online]. Available: http://www.abb.com/
[27] J. M. Guerrero, J. Matas, L. G. De Vicuña, M. Castilla, and J. Miret, "Wireless-control strategy for parallel operation of distributed-generation inverters," *IEEE Trans. Ind. Electron.*, vol. 53, no. 5, pp. 1461–1470, Oct. 2006.
[28] J. He, Y. W. Li, J. M. Guerrero, F. Blaabjerg, and J. C. Vasquez, "An islanding microgrid power sharing approach using enhanced virtual impedance control scheme," *IEEE Trans. Power Electron.*, vol. 28, no. 11, pp. 5272–5282, Nov. 2013.
[29] M. Ciobotaru, V. G. Agelidis, R. Teodorescu, and F. Blaabjerg, "Accurate and less-disturbing active antiislanding method based on PLL for grid-connected converters," *IEEE Trans. Power Electron.*, vol. 25, no. 6, pp. 1576–1584, Jun. 2010.
[30] *Voltage Characteristics of Electricity Supplied by Public Distribution System*, Standard EN 50160:2004, 2004.
[31] P. Rodriguez, J. Pou, J. Bergas, J. I. Candela, R. P. Burgos, and D. Boroyevich, "Decoupled double synchronous reference frame PLL for power converters control," *IEEE Trans. Power Electron.*, vol. 22, no. 2, pp. 584–592, Mar. 2007.
[32] S. Gkavanoudis and C. Demoulias, "A combined fault ride-through and power smoothing control method for full-converter wind turbines employing supercapacitor energy storage system," *Elect. Power Syst. Res.*, vol. 106, pp. 62–72, Jan. 2014.
[33] M. Ciobotaru, R. Teodorescu, and F. Blaabjerg, "A new single-phase PLL structure based on second order generalized integrator," in *Proc. IEEE 37th Power Electron. Spec. Conf.*, 2006, pp. 1–6.
[34] P. Rodríguez, A. Luna, R. S. Muñoz-Aguilar, I. Etxeberria-Otadui, R. Teodorescu, and F. Blaabjerg, "A stationary reference frame grid synchronization system for three-phase grid-connected power converters under adverse grid conditions," *IEEE Trans. Power Electron.*, vol. 27, no. 1, pp. 99–112, Jan. 2012.
[35] Maxwell Technologies, *Maxwell BOOSTCAP Ultracapacitors—Small Module Technical Papers*. (2013). [Online]. Available: http://www.maxwell.com/products/ultracapacitors/

Konstantinos O. Oureilidis (M'07) was born in 1984. He received the Dipl. and Ph.D. degrees in electrical engineering from the Aristotle University of Thessaloniki, Thessaloniki, Greece, in 2008 and 2015, respectively.

He is currently a Researcher in the Electrical Machines Laboratory, Department of Electrical and Computer Engineering, Aristotle University of Thessaloniki. His research interests include the fields of power electronics, distributed generation, power system protection, and renewable energy sources.

Charis S. Demoulias (M'96–SM'11) was born in 1961. He received the Dipl. and Ph.D. degrees in electrical engineering from the Aristotle University of Thessaloniki, Thessaloniki, Greece, in 1984 and 1991, respectively.

He is currently an Assistant Professor in the Electrical Machines Laboratory, Department of Electrical and Computer Engineering, Aristotle University of Thessaloniki. His research interests include the fields of power electronics, harmonics, electric motion systems, and renewable energy sources.